Progress In Electromagnetics Research M, Vol. 58, 43–55, 2017

Characteristic Analysis of Phase Glint in InSAR Image Processing

Jing-Ke Zhang[1, *], Da-Hai Dai[2], Zong-Feng Qi[1], Yong-Hu Zeng[1], and Lian-Dong Wang[1]

Abstract—This paper investigates the phase glint problem involved in interferometric synthetic aperture radar (InSAR) image processing, which refers to the multiple scatterer interference of a single pixel, and studies the distribution of interferometric phase in the case of double scatterer interference. It is found that the value range of the observed interferometric phase is related to several factors including the complex scattering coefficient ratio and interferometric phase difference between the elementary scatterers, and no matter what values of interferometric phases of elementary scatterers are taken, the range of interferometric phase of phase glint is always 2π. This paper also briefly analyzes the impact of phase glint on classical InSAR image processing and man-made target height retrieval, and it is concluded that the phase glint will induce significant height estimating error. Simulation and real data results verify the conclusion.

1. INTRODUCTION

Synthetic aperture radar (SAR) provides the full ability of acquiring high resolution radar images independent of sunlight illumination and weather conditions and is a well-proven technique for many military and civilian remote sensing fields [1–6]. However, conventional SAR imagery is a projection of observed scene from three-dimensional (3D) scene scattering properties onto the two-dimensional (2D) range-azimuth plane, which makes the interpretation of SAR image extremely difficult, especially for the man-made target [7, 8].

With the introduction of interferometric processing technique, some derived techniques, including InSAR [9], differential InSAR (DInSAR) [10], and polarimetric InSAR (PolInSAR) [11, 12], are developed, among which InSAR is a technique that obtains terrain digital elevation map (DEM) by coherently processing two images acquired from slightly different views. Although InSAR has achieved great success in various remote sensing applications, it cannot be applied in the 3D reconstruction of man-made targets, considering that the widely accepted assumption that a given pixel is dominated by scattering from a single height [9] is usually violated in many cases such as man-made target reconstruction. In fact, multiple scatterers with different heights may be mapped in the same pixel [13], which will produce a chaotic observed interferometric phase. We refer the effect to phase glint in this paper. Phase glint usually makes the results produced by classical InSAR image processing unacceptable. In [14] and [15], the authors analyze the impact of phase glint on the man-made height estimation and propose a method of detecting the existence of phase glint by using the pixel magnitudes corresponding to two coherent SAR images. In [16], based on the difference between the interferometric phases corresponding to different polarizations, a novel method of detecting phase glint is introduced. In [17] and [18], the detection methods of multiple scatterer interference based on differential SAR tomography are studied. However, the detailed distribution of the interferometric phase of phase glint along with the variety of the characteristic of the elementary scatterers is still lack of research.

Received 16 March 2017, Accepted 7 June 2017, Scheduled 27 June 2017

* Corresponding author: Jing-Ke Zhang (zhangjk1025@163.com).

[1] State Key Laboratory of Complex Electromagnetic Environment Effects on Electronics and Information System, Luoyang 471000, China. [2] State Key Laboratory of Complex Electromagnetic Environment Effects on Electronics and Information System, National University of Defense Technology, Changsha 410073, China.

This paper is dedicated to deriving the detailed phase distribution characteristic of phase glint and presents a demonstration about the impact of phase glint on two typical applications, i.e., classical InSAR image processing and man-made target height retrieval, by processing the simulated and real collected InSAR data. The paper is organized as follows. Section 2 introduces the concept and establishes the mathematic model. In Section 3, we derive the detailed distribution of the interferometric phase of phase glint and concisely analyze the impact of phase glint on classical InSAR image processing and man-made target height retrieval. In Section 4, simulation and real data results are presented to verify the validy of the theoretical analysis. Finally, conclusions are presented in Section 5.

2. PROBLEM FORMULATION

Without loss of generality, we consider InSAR system operating with single-pass mode. The raw data are focused on two SAR complex images, and the slave image is registered to the master image.

If there are N elementary scatterers located in an arbitrary pixel, the scattering response of the pixel can be expressed as

$$C_m = \sum_{k=1}^{N} A_k e^{\mathrm{j}\varphi_{mk}} \tag{1}$$

$$C_s = \sum_{k=1}^{N} A_k e^{\mathrm{j}\varphi_{sk}} \tag{2}$$

where A_k is the complex scattering coefficient of the kth scatterer; subscripts m and s represent the master and slave channel of InSAR system respectively; φ_{mk} and φ_{sk} denote the phases corresponding to the distances between the kth scatterer and the master and slave channels, respectively.

Then, the interferometric phase of the pixel can be written as

$$\Delta\varphi_{\mathrm{C}} = \arg\left(C_m C_s^*\right) \tag{3}$$

where superscripts $*$ represents conjunction operator. Obviously, when $\varphi_{mk} - \varphi_{sk} \neq \varphi_{mp} - \varphi_{sp} + 2k\pi$, $k, p \in \mathbb{Z}$, $k \neq p$, the interferometric phase φ_{C} varies with A_k and may be not equal to the interferometric phase of any elementary scatterer of the pixel, so $\Delta\varphi_{\mathrm{C}}$ cannot reflect the height of any elementary scatterer.

For the sake of simplify, we assume that the phase glint is caused by two elementary scatterers, A and B. The complex scattering coefficient ratio (CSCR) of B to A is $\rho\exp(\mathrm{j}\phi)$. Without loss of generality, we assume $0 \leq \rho \leq 1$ (if $\rho \geq 1$, we can obtain $0 \leq \rho \leq 1$ by interchanging A for B), and ϕ is uniformly distributed between $-\pi$ and π. Then, the scattering response of the pixel can be expressed as

$$S_m = A\exp\left(\mathrm{j}\varphi_{m\mathrm{A}}\right)\left(1+\rho\exp\left(\mathrm{j}\left(\phi+\varphi_{m\mathrm{B}}-\varphi_{m\mathrm{A}}\right)\right)\right) \tag{4}$$

$$S_s = A\exp\left(\mathrm{j}\varphi_{s\mathrm{A}}\right)\left(1+\rho\exp\left(\mathrm{j}\left(\phi+\varphi_{s\mathrm{B}}-\varphi_{s\mathrm{A}}\right)\right)\right) \tag{5}$$

where A is the complex scattering coefficient of scatterer A. Setting $\phi' = \phi + \varphi_{s\mathrm{B}} - \varphi_{s\mathrm{A}}$, $\Delta\varphi_{\mathrm{A}} = \varphi_{m\mathrm{A}} - \varphi_{s\mathrm{A}}$, $\Delta\varphi_{\mathrm{B}} = \varphi_{m\mathrm{B}} - \varphi_{s\mathrm{B}}$, $\Delta\varphi_{\mathrm{BA}} = \Delta\varphi_{\mathrm{B}} - \Delta\varphi_{\mathrm{A}}$, and without the consideration of phase wrapping, the interferometric phase of phase glint can be expressed as

$$\Delta\varphi_{\mathrm{C}} = \arg\left(S_m S_s^*\right) = \Delta\varphi_{\mathrm{A}} + \arg\left(\left(1+\rho\exp\left(\mathrm{j}\left(\phi'+\Delta\varphi_{\mathrm{BA}}\right)\right)\right)\left(1+\rho\exp\left(-\mathrm{j}\phi'\right)\right)\right) \tag{6}$$

where $\Delta\varphi_{\mathrm{A}}$ and $\Delta\varphi_{\mathrm{B}}$ denote the interferometric phases of A and B, respectively.

Equation (6) can be expanded as

$$\Delta\varphi_{\mathrm{C}} = \Delta\varphi_{\mathrm{A}} + \tan^{-1}\left(\frac{\rho\sin\left(\phi'+\Delta\varphi_{\mathrm{BA}}\right)-\rho\sin\phi'+\rho^2\sin\Delta\varphi_{\mathrm{BA}}}{1+\rho\cos\left(\phi'+\Delta\varphi_{\mathrm{BA}}\right)+\rho\cos\phi'+\rho^2\cos\Delta\varphi_{\mathrm{BA}}}\right) \tag{7}$$

From Eq. (7), it can be seen that the interferometric phase of phase glint is related to the interferometric phases $\Delta\varphi_{\mathrm{A}}$ and $\Delta\varphi_{\mathrm{B}}$, the interferometric phase difference $\Delta\varphi_{\mathrm{BA}}$, and the CSCR ($\rho\exp(\mathrm{j}\phi)$) of B to A.

3. MAIN RESULTS

3.1. Distribution Characteristic of Interferometric Phase

In this section, we will derive the detailed distribution of interferometric phase of phase glint. For given positions of scatterers A and B, the interferometric phase $\Delta\varphi_{\mathrm{C}}$ is the function of parameters ρ and ϕ. Setting $\Delta\varphi_{\mathrm{CA}} = \Delta\varphi_{\mathrm{C}} - \Delta\varphi_{\mathrm{A}}$, we can obtain

$$f(\rho,\phi) = \tan(\Delta\varphi_{\mathrm{CA}}) = \frac{\rho\sin(\phi' + \Delta\varphi_{\mathrm{BA}}) - \rho\sin\phi' + \rho^2\sin\Delta\varphi_{\mathrm{BA}}}{1 + \rho\cos(\phi' + \Delta\varphi_{\mathrm{BA}}) + \rho\cos\phi' + \rho\cos\Delta\varphi_{\mathrm{BA}}} \tag{8}$$

From Appendix A, it can be concluded that

$$\frac{df^2(\rho,\phi)}{d\phi^2} = \begin{cases} \dfrac{-2\left(\rho-\rho^3\right)\sin\left(\Delta\varphi_{\mathrm{BA}}/2\right)}{a^2} & \phi = -\frac{\Delta\varphi_{\mathrm{BA}}}{2} + \varphi_{\mathrm{sA}} - \varphi_{\mathrm{sB}} \\ \dfrac{2\left(\rho-\rho^3\right)\sin\left(\Delta\varphi_{\mathrm{BA}}/2\right)}{a^2} & \phi = \pi - \frac{\Delta\varphi_{\mathrm{BA}}}{2} + \varphi_{\mathrm{sA}} - \varphi_{\mathrm{sB}} \end{cases} \tag{9}$$

where $-\frac{\Delta\varphi_{\mathrm{BA}}}{2} + \varphi_{\mathrm{sA}} - \varphi_{\mathrm{sB}}$ and $\pi - \frac{\Delta\varphi_{\mathrm{BA}}}{2} + \varphi_{\mathrm{sA}} - \varphi_{\mathrm{sB}}$ is the extreme points of $f(\rho,\phi)$ with respect to ϕ.

According to $a^2 > 0$ and $\rho - \rho^3 \geq 0$, the polarity of Eq. (9) is only dominated by $\sin(\Delta\varphi_{\mathrm{BA}}/2)$, so we can obtain conclusions as follows:

(1) $\sin(\Delta\varphi_{\mathrm{BA}}/2) \geq 0$, i.e., $\Delta\varphi_{\mathrm{BA}} \in (0, 2\pi) + 4k\pi,\ k \in \mathbf{Z}$. When $\phi = \pi - \frac{\Delta\varphi_{\mathrm{BA}}}{2} + \varphi_{\mathrm{sA}} - \varphi_{\mathrm{sB}}$, $f(\rho,\phi)$ has local minimum value because of $\frac{df^2(\rho,\phi)}{d\phi^2} > 0$. Moreover, $\tan(\cdot)$ is monotone increasing function, so $\Delta\varphi_{\mathrm{C}}$ has local minimum value

$$\Delta\varphi_{\mathrm{C\_min}} = \Delta\varphi_{\mathrm{A}} - 2\tan^{-1}\left(\frac{\rho\sin\left(\Delta\varphi_{\mathrm{BA}}/2\right)}{1-\rho\cos\left(\Delta\varphi_{\mathrm{BA}}/2\right)}\right) \tag{10}$$

When $\phi = -\frac{\Delta\varphi_{\mathrm{BA}}}{2} + \varphi_{\mathrm{sA}} - \varphi_{\mathrm{sB}}$, $\Delta\varphi_{\mathrm{C}}$ has local maximum value

$$\Delta\varphi_{\mathrm{C\_max}} = \Delta\varphi_{\mathrm{A}} + 2\tan^{-1}\left(\frac{\rho\sin\left(\Delta\varphi_{\mathrm{BA}}/2\right)}{1+\rho\cos\left(\Delta\varphi_{\mathrm{BA}}/2\right)}\right) \tag{11}$$

(2) $\sin(\Delta\varphi_{\mathrm{BA}}/2) \leq 0$, i.e., $\Delta\varphi_{\mathrm{BA}} \in (-2\pi, 0) + 4k\pi$. When $\phi = \pi - \frac{\Delta\varphi_{\mathrm{BA}}}{2} + \varphi_{\mathrm{sA}} - \varphi_{\mathrm{sB}}$, $f(\rho,\phi)$ has maximal value. Because $\frac{df^2(\rho,\phi)}{d\phi^2} < 0$, $\Delta\varphi_{\mathrm{C}}$ has local maximal value

$$\Delta\varphi_{\mathrm{C\_max}} = \Delta\varphi_{\mathrm{A}} - 2\tan^{-1}\left(\frac{\rho\sin\left(\Delta\varphi_{\mathrm{BA}}/2\right)}{1-\rho\cos\left(\Delta\varphi_{\mathrm{BA}}/2\right)}\right) \tag{12}$$

When $\phi = -\frac{\Delta\varphi_{\mathrm{BA}}}{2} + \varphi_{\mathrm{sA}} - \varphi_{\mathrm{sB}}$, $\Delta\varphi_{\mathrm{C}}$ has local minimum value

$$\Delta\varphi_{\mathrm{C\_min}} = \Delta\varphi_{\mathrm{A}} + 2\tan^{-1}\left(\frac{\rho\sin\left(\Delta\varphi_{\mathrm{BA}}/2\right)}{1+\rho\cos\left(\Delta\varphi_{\mathrm{BA}}/2\right)}\right) \tag{13}$$

If $\Delta\varphi_{\mathrm{C\_max}}$ and $\Delta\varphi_{\mathrm{C\_min}}$ are regarded as the functions of ρ, one can obtain

$$\Delta\varphi_{\mathrm{C\_max}}(\rho) = \begin{cases} \Delta\varphi_{\mathrm{A}} + 2\tan^{-1}\left(\dfrac{\rho\sin(\Delta\varphi_{\mathrm{BA}/2})}{1+\rho\cos(\Delta\varphi_{\mathrm{BA}/2})}\right) & \Delta\varphi_{\mathrm{BA}} \in (0,2\pi) + 4k\pi \\ \Delta\varphi_{\mathrm{A}} - 2\tan^{-1}\left(\dfrac{\rho\sin(\Delta\varphi_{\mathrm{BA}/2})}{1-\rho\cos(\Delta\varphi_{\mathrm{BA}/2})}\right) & \Delta\varphi_{\mathrm{BA}} \in (-2\pi,0) + 4k\pi \end{cases} \tag{14}$$

$$\Delta\varphi_{\mathrm{C\_min}}(\rho) = \begin{cases} \Delta\varphi_{\mathrm{A}} - 2\tan^{-1}\left(\dfrac{\rho\sin(\Delta\varphi_{\mathrm{BA}/2})}{1-\rho\cos(\Delta\varphi_{\mathrm{BA}/2})}\right) & \Delta\varphi_{\mathrm{BA}} \in (0,2\pi) + 4k\pi \\ \Delta\varphi_{\mathrm{A}} + 2\tan^{-1}\left(\dfrac{\rho\sin(\Delta\varphi_{\mathrm{BA}/2})}{1+\rho\cos(\Delta\varphi_{\mathrm{BA}/2})}\right) & \Delta\varphi_{\mathrm{BA}} \in (-2\pi,0) + 4k\pi \end{cases} \tag{15}$$

Equations (14) and (15) are named as the maximal and minimum value curves in the following discussion.

According to Appendix B, for the case of $0 \le \rho \le 1$, the value range of $\Delta\varphi_{\mathrm{C}}$ can be expressed as

$$\Delta\varphi_{\mathrm{C}} \in \begin{cases} \left[\Delta\varphi_{\mathrm{A}} + \dfrac{\Delta\varphi'_{\mathrm{BA}}}{2} - \pi, \Delta\varphi_{\mathrm{A}} + \dfrac{\Delta\varphi'_{\mathrm{BA}}}{2}\right], & \Delta\varphi_{\mathrm{BA}} \in (0, 2\pi) + 4k\pi \\ \left[\Delta\varphi_{\mathrm{A}} + \dfrac{\Delta\varphi'_{\mathrm{BA}}}{2}, \Delta\varphi_{\mathrm{A}} + \dfrac{\Delta\varphi'_{\mathrm{BA}}}{2} + \pi\right], & \Delta\varphi_{\mathrm{BA}} \in (-2\pi, 0) + 4k\pi \end{cases} \tag{16}$$

Similarly, when $\rho \ge 1$, $\rho' \exp(\mathrm{j}\phi')$ is defined as the CSCR of B to A, that is $0 \le \rho' \le 1$. It also can be concluded that

$$\Delta\varphi_{\mathrm{C}} \in \begin{cases} \left[\varphi_{\mathrm{B}} - \dfrac{\Delta\varphi'_{\mathrm{BA}}}{2}, \Delta\varphi_{\mathrm{B}} - \dfrac{\Delta\varphi'_{\mathrm{BA}}}{2} + \pi\right], & \Delta\varphi_{\mathrm{BA}} \in (0, 2\pi) + 4k\pi \\ \left[\Delta\varphi_{\mathrm{B}} - \dfrac{\Delta\varphi'_{\mathrm{BA}}}{2} - \pi, \Delta\varphi_{\mathrm{B}} - \dfrac{\Delta\varphi'_{\mathrm{BA}}}{2}\right], & \Delta\varphi_{\mathrm{BA}} \in (-2\pi, 0) + 4k\pi \end{cases} \tag{17}$$

In summary, if elementary scatterers A and B are located in a single pixel of SAR image, along with the change of $\rho \in [0 + \infty)$ and $\phi \in [-\pi, \pi]$, the value range of interferometric phase of the corresponded pixel is

$$\Delta\varphi_{\mathrm{C}} \in \left[\Delta\varphi_{\mathrm{A}} + \frac{\Delta\varphi'_{\mathrm{BA}}}{2} - \pi, \Delta\varphi_{\mathrm{A}} + \frac{\Delta\varphi'_{\mathrm{BA}}}{2}\right] \cup \left[\Delta\varphi_{\mathrm{B}} - \frac{\Delta\varphi'_{\mathrm{BA}}}{2}, \Delta\varphi_{\mathrm{B}} - \frac{\Delta\varphi'_{\mathrm{BA}}}{2} + \pi\right], \ \Delta\varphi_{\mathrm{BA}} \in (0, 2\pi) + 4k\pi \tag{18}$$

$$\Delta\varphi_{\mathrm{C}} \in \left[\Delta\varphi_{\mathrm{B}} - \frac{\Delta\varphi'_{\mathrm{BA}}}{2} - \pi, \Delta\varphi_{\mathrm{B}} - \frac{\Delta\varphi'_{\mathrm{BA}}}{2}\right] \cup \left[\Delta\varphi_{\mathrm{A}} + \frac{\Delta\varphi'_{\mathrm{BA}}}{2}, \Delta\varphi_{\mathrm{A}} + \frac{\Delta\varphi'_{\mathrm{BA}}}{2} + \pi\right], \ \Delta\varphi_{\mathrm{BA}} \in (-2\pi, 0) + 4k\pi \tag{19}$$

From Eqs. (18) and (19), we can conclude that the value range of interferometric phase $\Delta\varphi_{\mathrm{C}}$ in the case of double scatterer interference is related to the interferometric phases $\Delta\varphi_{\mathrm{A}}$ and $\Delta\varphi_{\mathrm{B}}$ of elementary scatterers, and the interferometric phase difference $\Delta\varphi_{\mathrm{BA}}$ between the elementary scatterers. However, no matter what values of $\Delta\varphi_{\mathrm{A}}$, $\Delta\varphi_{\mathrm{B}}$ or $\Delta\varphi_{\mathrm{BA}}$ are taken, along with the change of ρ and ϕ, the dynamic range of interferometric phase $\Delta\varphi_{\mathrm{C}}$ is always 2π. Moreover, in some cases, the value of $\Delta\varphi_{\mathrm{C}}$ exceeds the span decided by $\Delta\varphi_{\mathrm{A}}$ and $\Delta\varphi_{\mathrm{B}}$.

3.2. Impact on Classical InSAR Image Processing

In classical InSAR image processing, the extracted interferometric phase is always a wrapped phase, which can be expressed as

$$\Delta\varphi_{\mathrm{W}} = \mathrm{wrap}\left(\Delta\varphi\right) \tag{20}$$

where wrap$(\cdot)$ defines a wrapping operator; $\Delta\varphi$ is unwrapped phase; $\Delta\varphi_{\mathrm{W}}$ is the wrapped phase of $\Delta\varphi$ and $\Delta\varphi_{\mathrm{W}} \in [-\pi, \pi]$. If the number of wrapped cycles is n, the relationship between $\Delta\varphi_{\mathrm{W}}$ and $\Delta\varphi$ can be express as

$$\Delta\varphi_{\mathrm{W}} = \Delta\varphi - 2n\pi \tag{21}$$

Phase unwrapping is any technique that permits retrieving the unwrapped phase $\Delta\varphi$ from the wrapped phase $\Delta\varphi_{\mathrm{W}}$ in InSAR image processing. Most phase unwrapping algorithms are based on the hypothesis that the absolute value of phase gradient of adjacent pixels is less than π. According to the analysis of Section 3.1, the interferometric phase of phase glint varies with CSCR, which may lead to the absolute value of phase gradient greater than π, i.e., the unwrapped phase may be incorrect. With the flat phase removed, phase filtering, phase unwrapping and the flat phase compensated, if the ultimate interferometric phase is $\Delta\varphi'$, the retrieved height can be expressed as [9]

$$h' \approx H - R\cos\left(\varepsilon + \sin^{-1}\left(\frac{-\lambda\Delta\varphi'}{2\pi B}\right)\right) \tag{22}$$

where H denotes the height of platform, R the distance between corresponding pixel and InSAR master channel antenna, B the baseline length, ε the angle the baseline makes with respect to a reference horizontal plane (see Fig. 1), and λ the wavelength. Because $\Delta\varphi'$ is not equal to the interferometric phase of any elementary scatterer, the retrieved height h' cannot reflect the real height of any elementary scatterer.

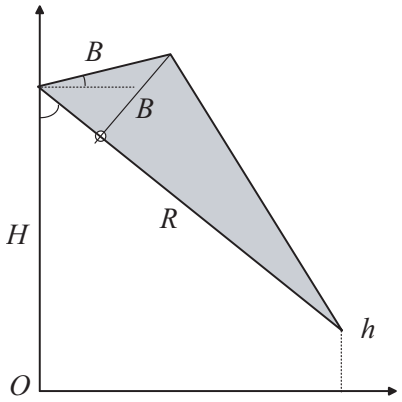

Figure 1. System geometry of InSAR.

3.3. Impact on Man-Made Target Height Retrieval

In the case of man-made target reconstruction, because the scattering response can be characterized as a superposition of a set of discrete scatterers, conventional phase unwrapping algorithms cannot work effectively. In order to estimate the man-made target height using single-pass polarimetric interferometric SAR system, [16] proposes a novel method utilizing the interferometric phases of the scatterer couples.

If the unwrapped interferometric phase of a couple of scatterer of InSAR images is $\Delta\varphi$, it can be split into two terms

$$\Delta\varphi = \frac{2\pi}{\lambda} B_\perp \frac{\Delta R}{R_0 \tan\theta} + \frac{2\pi}{\lambda} B_\perp \frac{h}{R_0 \sin\theta} \tag{23}$$

where $B_\perp$ is the perpendicular baseline length, R_0 the range value of the middle scene, θ the looking angle, and h the height of the scatterer (see Fig. 1). The first term is referred to as flat earth phase, which can be calculated in accordance with the imaging geometry. With the flat phase removed, scatterer height can be directly estimated from the unwrapped interferometric phase $\Delta\varphi'$

$$h = \frac{\Delta\varphi' \lambda R_0 \sin\theta}{2\pi B_\perp} \tag{24}$$

It is obvious that the maximum unambiguity height value is $h_{uamp} = \lambda R_0 \sin\theta / B_\perp$.

Without the consideration of the existence of phase glint, a flowchart of man-made target height retrieval used in [16] is shown as Fig. 2. Firstly, the flat phase is removed between the master image and slave image. Then, based on the scattering center model, the scattering centers are extracted from the master and slave images. Next, the interferometric phases of corresponding scatterer couples are obtained. In the man-made target height retrieval, the imaged scene is usually very small, and the maximum unambiguity height is much higher than the target height for most interferometric system configurations, implying that the target height can be directly estimated from the extracted interferometric phases. Finally, the target height is retrieved from the extracted interferometric phases as in Eq. (24). It should be pointed out that the retrieved height is a relative height. According to Section 3.1, if the extracted scatterer couples include those caused by phase glint, especially in the case that the interferometric phase exceeds the span decided by the elementary scatterers, the retrieved height will deviate greatly from the real one.

4. EXPERIMENTAL EXAMPLES

To further analyses the distribution of interferometric phase and impact of the phase glint on InSAR image processing, simulation and real data experiment results are presented in the section. Section 4.1 verifies the distribution characteristics of interferometric phase of phase glint, which are presented in Section 3.1. Section 4.2 considers the classical InSAR image processing results of phase glint. The

Table 1. Parameters of InSAR system.

System Parameter	Value
Carrier frequency/GHz	10
Height of airplane/m	8000
Velocity of airplane/(m/s)	125
Looking angle/(°)	45
Range resolution/m	1
Azimuth resolution/m	1

parameters of InSAR system in Sections 4.1 and 4.2 are listed in Table 1. In order to demonstrate the impact of phase glint on man-made target height retrieval, real data experiment is presented in Section 4.3.

4.1. Validation of Distribution of Interferometric Phase

In simulation I, scatterers A and B are located at $(0, 8000, 0)$ m and $(0, 8010, 10)$ m, respectively, so it can be obtained that $\Delta\varphi_{\mathrm{A}} = 0.037$ rad, $\Delta\varphi_{\mathrm{B}} = -0.4866$ rad and $\Delta\varphi_{\mathrm{BA}} = -\frac{\pi}{6} \in [-2\pi, 0]$. The span decided by the interferometric phases of the elementary scatterers is $[-0.4866, 0.037]$ rad. The distribution of $\Delta\varphi_{\mathrm{C}}$ when $0 \leq \rho \leq 1$ is shown in Fig. 3(a), and the value range is $[-0.2488, 2.9168]$ rad, which is consistent with the theoretical value $[\Delta\varphi_{\mathrm{A}} + \frac{\Delta\varphi_{\mathrm{BA}}}{2}, \Delta\varphi_{\mathrm{A}} + \frac{\Delta\varphi_{\mathrm{BA}}}{2} + \pi]$. Fig. 3(b) and Fig. 3(c) represent the maximal and minimum value curves which are defined in Section 3.1, respectively. One can see that the maximal e and minimum value curves are the monotone increasing function and monotone decreasing function of ρ, respectively. The distribution of $\Delta\varphi_{\mathrm{C}}$ when $\rho \geq 1$ is shown in Fig. 3(d), and the value range is $[-3.3664, -0.2448]$ rad. From Fig. 3(e) and Fig. 3(f), it can be seen that the maximal value of $\Delta\varphi_{\mathrm{C}}$ is -0.2448 rad, and the minimum value is -3.3664 rad. Form Fig. 3(a) and Fig. 3(d), one can conclude that the value interval of $\Delta\varphi_{\mathrm{C}}$ is $[-3.3664, 2.9168]$ rad which obviously exceeds the span decided by interferometric phases of the elementary scatterers, and the dynamic range of $\Delta\varphi_{\mathrm{C}}$ is 2π, which are consistent with the theoretical value as shown in Eq. (19).

In simulation II, the coordinates of scatterer A are $(0, 8000, 89.5)$ m, and the coordinates of scatterer

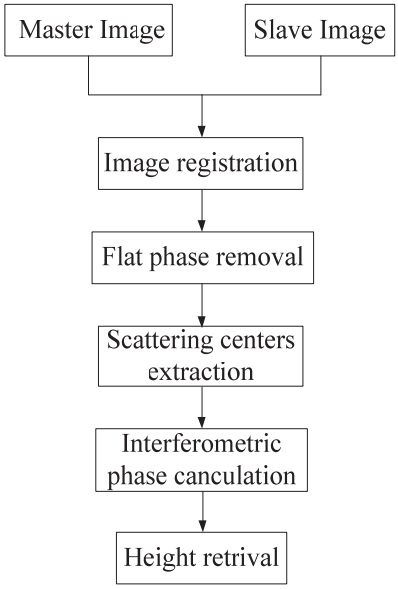

Figure 2. Flow chart of man-made height retrieval based on InSAR system.

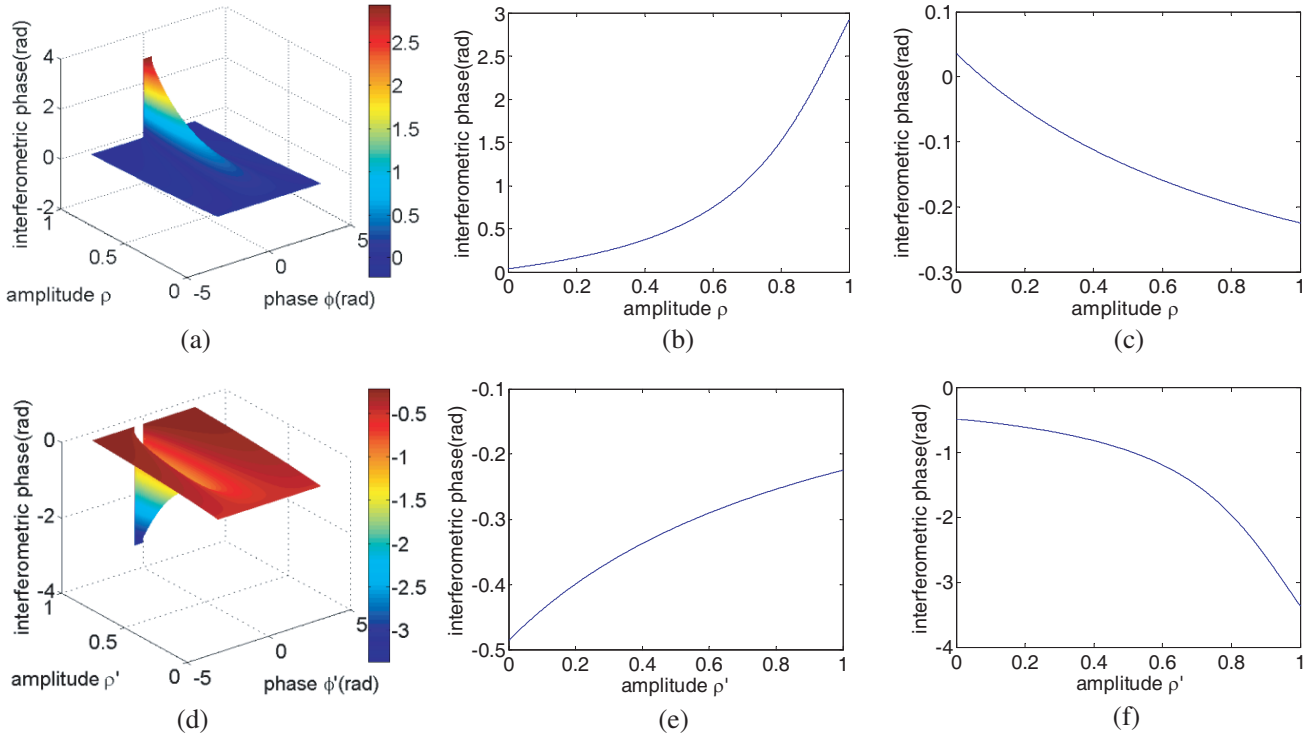

Figure 3. Distribution of interferometric phase of simulation I. (a) Interferometric phase versus ρ and ϕ ($0 \leq \rho \leq 1$). (b) The maximal value curve of interferometric phase versus ρ ($0 \leq \rho \leq 1$, $\phi = 0.299$ rad). (c) The minimum value curve of interferometric phase versus ρ ($0 \leq \rho \leq 1$, $\phi = -2.8426$ rad). (d) Interferometric phase versus ρ' and ϕ' ($\rho \geq 1$). (e) The maximal value curve of interferometric phase versus ρ' ($\rho \geq 1$, $\phi' = 2.8426$ rad). (f) The minimum value curve of interferometric phase versus ρ' ($\rho \geq 1$, $\phi' = -0.299$ rad).

B are $(0, 7910.5, 0)$ m, which means $\Delta\varphi_{\mathrm{A}} = -2.319$ rad, $\Delta\varphi_{\mathrm{B}} = 2.3935$ rad and $\Delta\varphi_{\mathrm{BA}} = 1.5\pi \in [0, 2\pi]$. From Fig. 4, one can conclude that the value range of $\Delta\varphi_{\mathrm{C}}$ is $[-3.3664, 2.9168]$ rad, and the dynamic range of $\Delta\varphi_{\mathrm{C}}$ is 2π, which are consistent with the theoretical value as shown in Eq. (18).

4.2. Classical InSAR Image Processing Results

In this part, two simulation experiments of airborne InSAR are presented to analyze the impact of phase glint on classical InSAR image process. Both simulation scenarios share the same terrain, which is a flat plane with an area 400 m × 400 m in both ground range direction and azimuth direction. Two group scatterers are set in both simulation experiments, and the coordinates are the same as in Section 4.1. The parameters ρ and ϕ of each simulation are shown in Table 2. In order to minimize the influence of the terrain to the interferometric phase of phase glint, the signal power to clutter power ratio (SCR) is set as 5 dB. Then, the classical image processing is applied to each simulation. The image results are shown as in Fig. 5 and Fig. 6, and the comparisons of the theoretical values and estimated values are shown in Table 2.

According to Table 2, the interferometric phase of each scatterer group of simulation III does not exceed the span decided by the elementary scatterers ($-0.1783 \in [-0.4866, 0.037]$ rad, $-0.2156 \in [-2.319, 2.3935]$ rad), and the height of each scatterer group is within the height of the elementary scatterers ($4.1 \in [0, 10]$ m,$49.4 \in [0, 89.5]$ m). From Fig. 5 and Table 2, one can conclude that the retrieved interferometric phase and height are consistent with the theoretical values. In this case, because of the retrieval height within the height interval of the elementary scatterers, the phase glint does not produce significant error for height retrieval. However, the retrieval height cannot reflect the real height of any elementary scatterers.

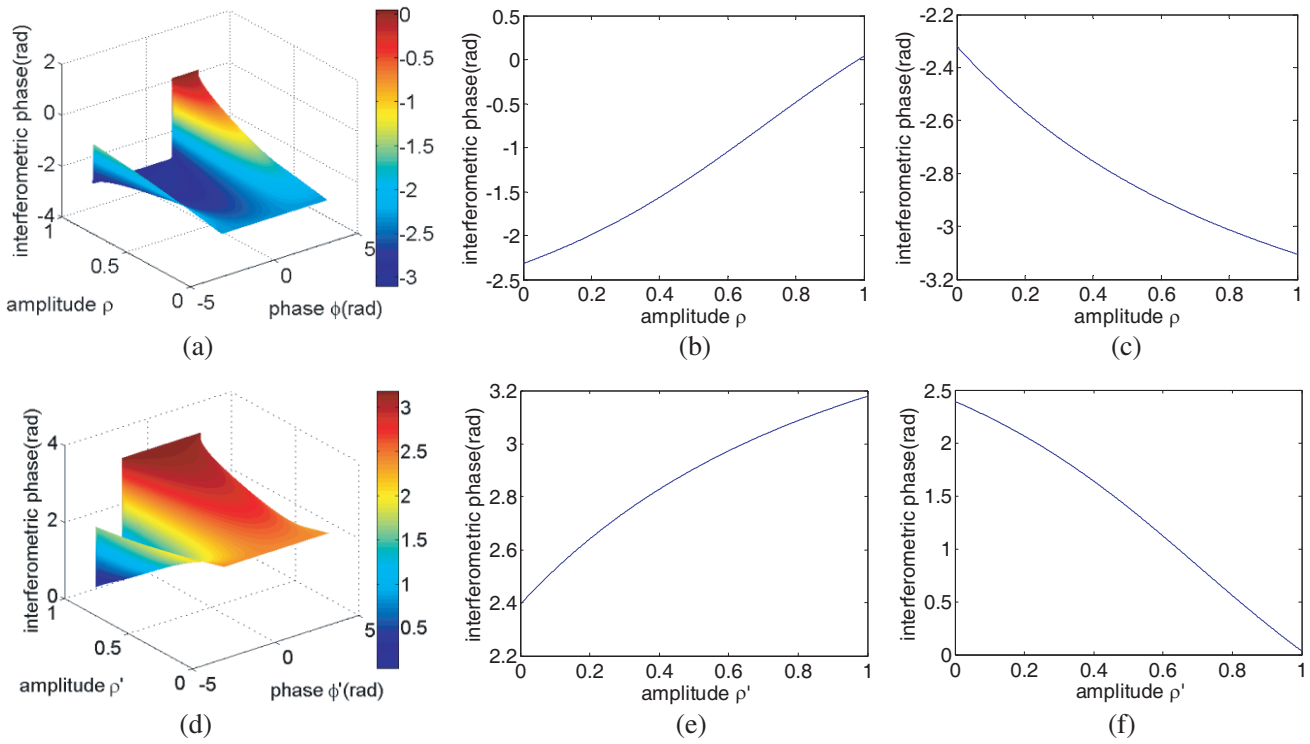

Figure 4. Distribution of interferometric phase of simulation II. (a) Interferometric phase versus ρ and $\phi(0 \le \rho \le 1)$. (b) The maximal value curve of interferometric phase versus ρ $(0 \le \rho \le 1, \phi = 2.3562\,\text{rad})$. (c) The minimum value curve of interferometric phase versus ρ $(0 \le \rho \le 1, \phi = -0.7853\,\text{rad})$. (d) Interferometric phase versus ρ' and ϕ' $(\rho \ge 1)$. (e) The maximal value curve of interferometric phase versus ρ' $(\rho \ge 1, \phi' = 0.7853\,\text{rad})$. (f) The minimum value curve of interferometric phase versus ρ' $(\rho \ge 1, \phi' = -2.3562\,\text{rad})$.

Table 2. Parameters setting and the comparison of the theoretical values and the estimated results of classical InSAR image processing.

		ρ	$\phi/(\text{rad})$	$\Delta\varphi_{\text{C}}/(\text{rad})$	$h/(\text{m})$	$\Delta\hat{\varphi}_{\text{C}}/(\text{rad})$	$\hat{h}/(\text{m})$
Simulation III	Scatterer group 1	0.7	−2.8426	−0.1783	4.1	−0.1747	4.04
	Scatterer group 2	0.9	2.3562	−0.2156	49.4	−0.2117	49.3
Simulation IV	Scatterer group 1	10/7	0.3	−1.5067	29.5	1.494	29.3
	Scatterer group 2	0.5	−0.7856	−2.83	99.3	3.462	−20.3

In simulation IV, the interferometric phases of both scatterer groups exceed the span decided by the elementary scatterers ($-1.5067 \notin [-0.4866, 0.037]\,\text{rad}$, $-2.83 \notin [-2.319, 2.3935]\,\text{rad}$), and the corresponding height of each scatterer group exceeds the height interval of the elementary scatterers ($29.5 \notin [0, 10]\,\text{m}$, $49.4 \notin [0, 89.5]\,\text{m}$). According to Fig. 6 and Table 2, the retrieved interferometric phase and height of the first scatterer group are approximate to the theoretical values, while the retrieved interferometric phase and height of the second scatterer group are different from the theoretical values. From Fig. 6 and Table 2, we can see that the retrieved interferometric phase of the second group is approximate to the wrapped value (3.4532 rad) of the theoretical value, because the absolute value of interferometric phase gradient between the second group and the adjacent terrain exceeds π, which results in that the interferometric phase of the second group is not unwrapped effectively and that the

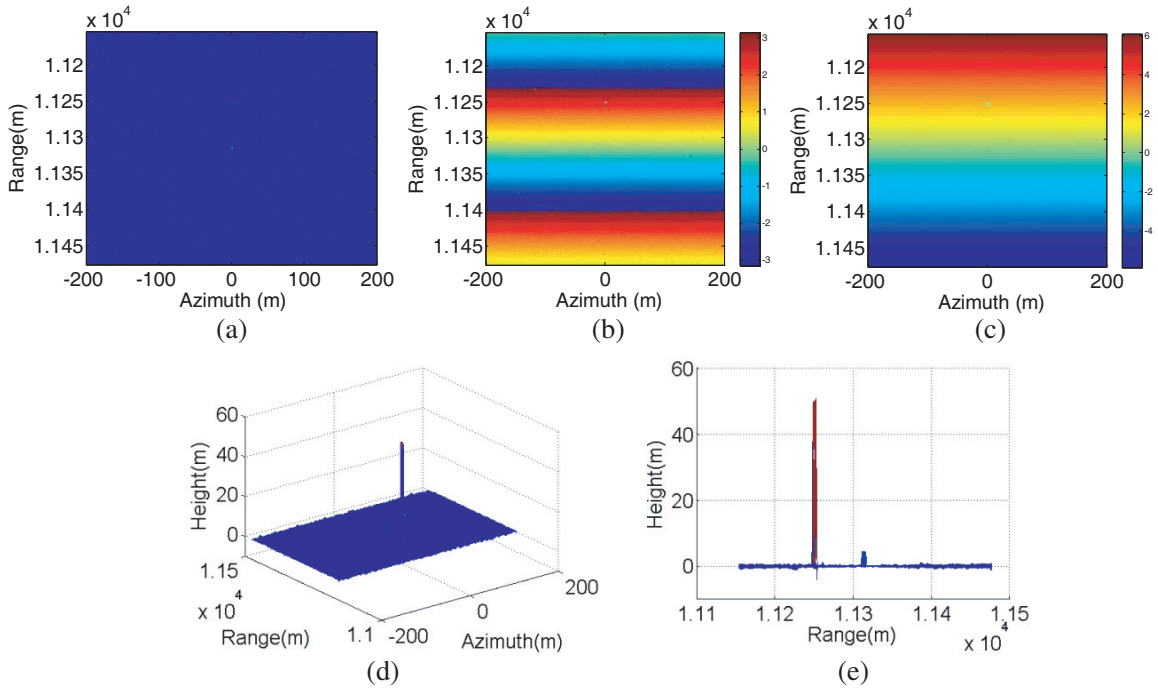

Figure 5. The InSAR image processing results of simulation III. (a) Master image. (b) Wrapped interferogram. (c) Unwrapped interferogram. (d) DEM. (e) Azimuth-height projection DEM.

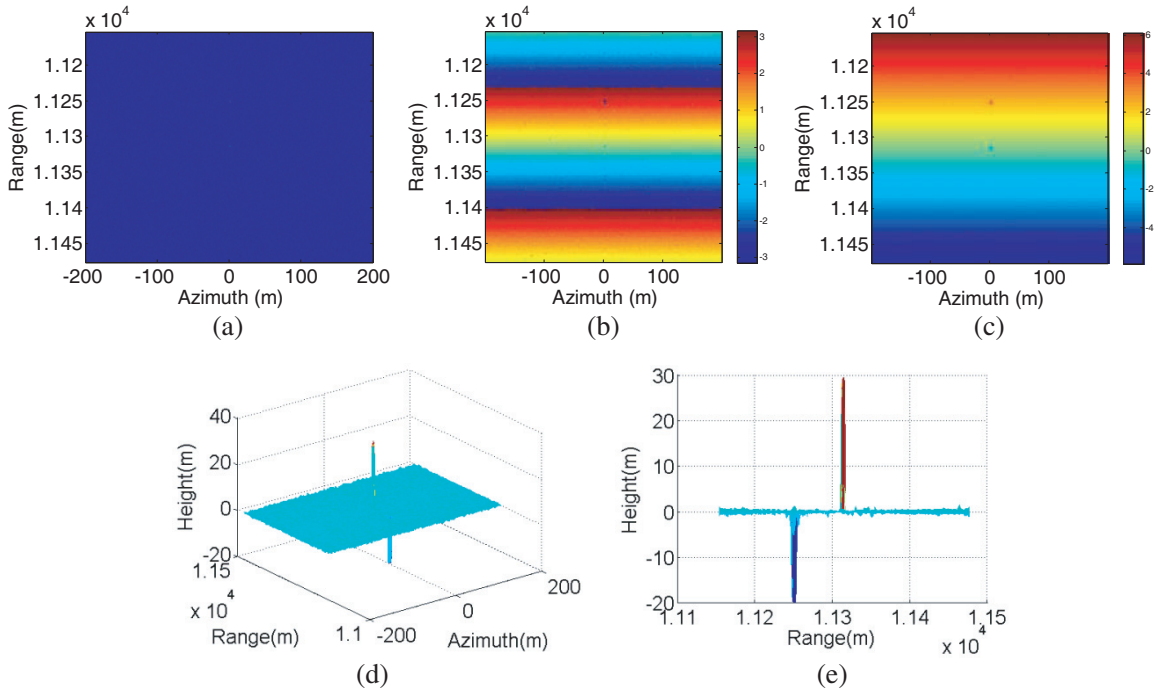

Figure 6. The InSAR image processing results of simulation IV. (a) Master image. (b) Wrapped interferogram. (c) Unwrapped interferogram. (d) DEM. (e) Azimuth-height projection DEM.

retrieval height is quite different from the real height of any elementary scatterer. In this case, the interferometric phase of phase glint exceeds the phase interval decided by the elementary scatterers, which will lead to serious height estimated error.

In sum, the interferometric phase of phase glint varies with the CSCR of elementary scatterers, and the retrieved height from the interferometric phase cannot reflect the real height of any elementary scatterer. When the interferometric phase exceeds the span decided by the interferometric phases of the elementary scatterers, it will produce serious height estimation error in classical InSAR image processing.

4.3. Man-Made Target Height Retrieval Results

To demonstrate the impact of phase glint on man-made height retrieval, we apply the method presented in Section 3.3 to real data provided by East China Research Institute of Electronic Engineering. The data are acquired with carrier frequency of 9.6 GHz in single pass bistatic mode over Lingshui County of China. The spatial resolutions in the slant range and azimuth direction are both 0.3 m. The interferometric baseline is about 1.22 m with its orientation angle $\varepsilon = 15.6°$. Considering that radar looking angle for the middle scene is about $\theta \approx 50.3°$ ($R_0 \approx 8.3$ km, and $H \approx 5.3$ km), we obtain the perpendicular baseline $B_\perp = 1$ m. The maximum unambiguity height is $h_{\text{uamp}} = 198$ m. For airplane target height retrieval, the unambiguity height is sufficient. We choose a slice of the real data, which corresponds to an airplane parked on the aerodrome. The real height of the airplane is about 11 m. Fig. 7 presents the SAR images of the airplane.

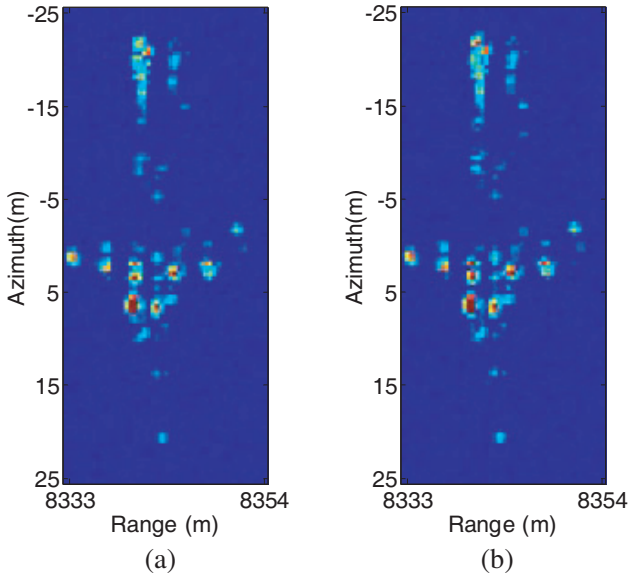

Figure 7. SAR images of an airplane. (a) Master image. (b) Slave image.

With the flat phase removed and the 2D ESPRIT technique [19] applied to the images, we obtain a set of scattering centers. The results are presented in Fig. 8(a), and the marker size indicates the intensity of the scatterer. From Fig. 8(a), it can be seen that the extracted scatterers clearly depict the shape of airplane in the 2D plane. Then, according to the interferometric phases of corresponding scatterer couple, the scatterer height is estimated as in Eq. (24). The results are presented in Figs. 8(b) and (c). We notice that the height difference between the estimates for the scatterers achieves 45 m which exceeds the real height, implying that the results are unreliable. It is because there exists phase glint caused by multiple scatterer interference in the airplane, and the interferometric phases of these scatterers cannot reflect the real height of the target.

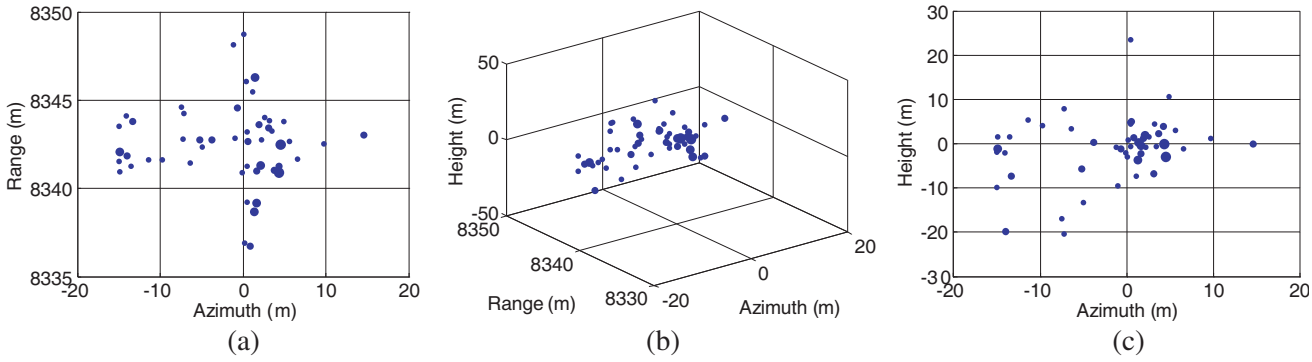

Figure 8. 3D reconstruction results for the airplane. (a) Range-azimuth projection map. (b) 3D representation of the scatterers. (c) Azimuth-height projection map.

5. CONCLUSION

In this paper, we investigate the phase glint problem caused by multiple scatterer interference of a single pixel in single-pass InSAR system. Our mathematic analysis indicates that the observed interferometric phase of phase glint is a chaotic value and varies with the CSCR between the elementary scatterers, which cannot reflect the real height of any elementary scatterer and may produce serious height estimating error. Simulation and real data experiment results verify the theoretical analysis. Our analysis and experimental results suggest that for height retrieval especially for man-made target, extra care is needed to account for the effects of phase glint caused by multiple scatterer interference.

Moreover, for the specialty of creating a chaotic interferometric in InSAR image processing, the phase glint can be utilized to develop three-dimension deceptive scene generation method against InSAR.

APPENDIX A.

This appendix will derive Equation (9). The first derivative of $f(\rho, \phi)$ which is shown as in Eq. (8) with respect to ϕ can be expressed as

$$\frac{df\left(\rho,\phi\right)}{d\phi} = \frac{\left(\rho-\rho^3\right)\left(\cos\left(\phi'+\Delta\varphi_{\mathrm{BA}}\right)-\cos\phi'\right)}{\left(1+\rho\cos\left(\phi'+\Delta\varphi_{\mathrm{BA}}\right)+\rho\cos\phi'+\rho\cos\Delta\varphi_{\mathrm{BA}}\right)^2} \tag{A1}$$

Let $\frac{df(\rho,\phi)}{d\phi} = 0$, and the extreme points of $f(\rho,\phi)$ are derived as $\phi = -\frac{\Delta\varphi_{\mathrm{BA}}}{2} + \varphi_{\mathrm{sA}} - \varphi_{\mathrm{sB}}$ and $\phi = \pi - \frac{\Delta\varphi_{\mathrm{BA}}}{2} + \varphi_{\mathrm{sA}} - \varphi_{\mathrm{sB}}$.

Substituting a for the denominator of the right of Eq. (A1), the second derivative of $f(\rho,\phi)$ with respect to φ can be written as

$$\frac{df^2\left(\rho,\phi\right)}{d\phi^2} = \frac{\left(\rho-\rho^3\right)\left(\left(\sin\phi'-\sin\left(\phi'+\Delta\varphi_{\mathrm{BA}}\right)\right)a-\left(\cos\left(\phi'+\Delta\varphi_{\mathrm{BA}}\right)-\cos\phi'\right)a'\right)}{a^2} \tag{A2}$$

where a' represents the derivative of a with respect to ϕ. When $\phi = -\frac{\Delta\varphi_{\mathrm{BA}}}{2} + \varphi_{\mathrm{sA}} - \varphi_{\mathrm{sB}}$ or $\phi = \pi - \frac{\Delta\varphi_{\mathrm{BA}}}{2} + \varphi_{\mathrm{sA}} - \varphi_{\mathrm{sB}}$, one can obtain that

$$\frac{df^2\left(\rho,\phi\right)}{d\phi^2} = \begin{cases} \dfrac{-2\left(\rho-\rho^3\right)\sin\left(\Delta\varphi_{\mathrm{BA}}/2\right)}{a} & \phi = -\dfrac{\Delta\varphi_{\mathrm{BA}}}{2} + \varphi_{\mathrm{sA}} - \varphi_{\mathrm{sB}} \\ \dfrac{2\left(\rho-\rho^3\right)\sin\left(\Delta\varphi_{\mathrm{BA}}/2\right)}{a} & \phi = \pi - \dfrac{\Delta\varphi_{\mathrm{BA}}}{2} + \varphi_{\mathrm{sA}} - \varphi_{\mathrm{sB}} \end{cases} \tag{A3}$$

APPENDIX B.

This appendix will derive the value range of $\Delta\varphi_{\mathrm{C}}$ for the case of $0 \le \rho \le 1$.

Setting $x = \frac{\rho\sin(\Delta\varphi_{\mathrm{BA}}/2)}{1+\rho\cos(\Delta\varphi_{\mathrm{BA}}/2)}$ and $y = \frac{\rho\sin(\Delta\varphi_{\mathrm{BA}}/2)}{1-\rho\cos(\Delta\varphi_{\mathrm{BA}}/2)}$, and substituting into $\Delta\varphi_{\mathrm{C_max}}(\rho)and\Delta\varphi_{\mathrm{C_min}}(\rho)$ which are expressed by Eqs. (14) and (15), respectively, the derivatives of $\Delta\varphi_{\mathrm{C\_max}}(\rho)$ and $\Delta\varphi_{\mathrm{C\_min}}(\rho)$ with respect to ρ can be expressed as

$$\Delta\varphi'_{\mathrm{C\_max}}(\rho) = \begin{cases} \dfrac{2\sin(\Delta\varphi_{\mathrm{BA}}/2)}{(1+x^2)(1+\rho\cos(\Delta\varphi_{\mathrm{BA}}/2))^2} & \Delta\varphi_{\mathrm{BA}} \in (0,2\pi)+4k\pi \\ -\dfrac{2\sin(\Delta\varphi_{\mathrm{BA}}/2)}{(1+y^2)(1-\rho\cos(\Delta\varphi_{\mathrm{BA}}/2))^2} & \Delta\varphi_{\mathrm{BA}} \in (-2\pi,0)+4k\pi \end{cases} \tag{B1}$$

$$\Delta\varphi'_{\mathrm{C}\_min}(\rho) = \begin{cases} -\dfrac{2\sin(\Delta\varphi_{\mathrm{BA}}/2)}{(1+y^2)(1-\rho\cos(\Delta\varphi_{\mathrm{BA}}/2))^2} & \Delta\varphi_{\mathrm{BA}} \in (0,2\pi)+4k\pi \\ \dfrac{2\sin(\Delta\varphi_{\mathrm{BA}}/2)}{(1+x^2)(1+\rho\cos(\Delta\varphi_{\mathrm{BA}}/2))^2} & \Delta\varphi_{\mathrm{BA}} \in (-2\pi,0)+4k\pi \end{cases} \tag{B2}$$

From Eqs. (B1) and (B2), it can be seen that $\Delta\varphi'_{\mathrm{C\_max}}(\rho) \geq 0$ and $\Delta\varphi'_{\mathrm{C\_min}}(\rho) \leq 0$ for arbitrary $\Delta\varphi_{\mathrm{BA}}$, i.e., $\Delta\varphi_{\mathrm{C\_max}}(\rho)$ is monotone increasing function while $\Delta\varphi_{\mathrm{C\_min}}(\rho)$ is monotone decreasing function of ρ. So, $\Delta\varphi_{\mathrm{C\_max}}(\rho)$ and $\Delta\varphi_{\mathrm{C\_min}}(\rho)$ have maximal value and minimum value, respectively, when $\rho = 1$, which are also the maximal and minimum values of $\Delta\varphi_{\mathrm{C}}$. Moreover, it can be concluded that $\min(\Delta\varphi_{\mathrm{C\_max}}(\rho)) = \max(\Delta\varphi_{\mathrm{C\_min}}(\rho)) = \Delta\varphi_{\mathrm{A}}$. In summary, the value range of $\Delta\varphi_{\mathrm{C}}(\rho,\varphi)$ is equal to the union of the range of $\Delta\varphi_{\mathrm{C\_max}}(\rho)$ and $\Delta\varphi_{\mathrm{C\_min}}(\rho)$. So, one can obtain

$$\max(\Delta\varphi_{\mathrm{C}}) = \Delta\varphi_{\mathrm{C\_max}}(1) = \begin{cases} \Delta\varphi_{\mathrm{A}} + 2\tan^{-1}\left(\dfrac{\sin(\Delta\varphi_{\mathrm{BA}}/2)}{1+\cos(\Delta\varphi_{\mathrm{BA}}/2)}\right) & \Delta\varphi_{\mathrm{BA}} \in (0,2\pi)+4k\pi \\ \Delta\varphi_{\mathrm{A}} - 2\tan^{-1}\left(\dfrac{\sin(\Delta\varphi_{\mathrm{BA}}/2)}{1-\cos(\Delta\varphi_{\mathrm{BA}}/2)}\right) & \Delta\varphi_{\mathrm{BA}} \in (-2\pi,0)+4k\pi \end{cases} \tag{B3}$$

$$\min(\Delta\varphi_{\mathrm{C}}) = \Delta\varphi_{\mathrm{C}\_min}(1) = \begin{cases} \Delta\varphi_{\mathrm{A}} - 2\tan^{-1}\left(\dfrac{\sin(\Delta\varphi_{\mathrm{BA}}/2)}{1-\cos(\Delta\varphi_{\mathrm{BA}}/2)}\right) & \Delta\varphi_{\mathrm{BA}} \in (0,2\pi)+4k\pi \\ \Delta\varphi_{\mathrm{A}} + 2\tan^{-1}\left(\dfrac{\sin(\Delta\varphi_{\mathrm{BA}}/2)}{1+\cos(\Delta\varphi_{\mathrm{BA}}/2)}\right) & \Delta\varphi_{\mathrm{BA}} \in (-2\pi,0)+4k\pi \end{cases} \tag{B4}$$

For a given $\Delta\varphi_{\mathrm{BA}}$, there is always a $\Delta\varphi'_{\mathrm{BA}} \in [-2\pi, 2\pi]$ satisfying $\Delta\varphi'_{\mathrm{BA}} = \Delta\varphi_{\mathrm{BA}} - 4k\pi$. According to submultiple angle formula of trigonometric functions

$$\tan^{-1}\left(\frac{\sin(\Delta\varphi_{\mathrm{BA}}/2)}{1-\cos(\Delta\varphi_{\mathrm{BA}}/2)}\right) = \begin{cases} \dfrac{\pi}{2} - \dfrac{\Delta\varphi'_{\mathrm{BA}}}{4} & \Delta\varphi_{\mathrm{BA}} \in (0,2\pi)+4k\pi \\ -\dfrac{\pi}{2} - \dfrac{\Delta\varphi'_{\mathrm{BA}}}{4} & \Delta\varphi_{\mathrm{BA}} \in (-2\pi,0)+4k\pi \end{cases} \tag{B5}$$

$$\tan^{-1}\left(\frac{\sin(\Delta\varphi_{\mathrm{BA}}/2)}{1+\cos(\Delta\varphi_{\mathrm{BA}}/2)}\right) = \frac{\Delta\varphi'_{\mathrm{BA}}}{4} \tag{B6}$$

Then, it can be concluded that

$$\Delta\varphi_{\mathrm{A}} - 2\tan^{-1}\left(\frac{\sin(\Delta\varphi_{\mathrm{BA}}/2)}{1-\cos(\Delta\varphi_{\mathrm{BA}}/2)}\right) = \begin{cases} \Delta\varphi_{\mathrm{A}} + \dfrac{\Delta\varphi'_{\mathrm{BA}}}{2} - \pi & \Delta\varphi_{\mathrm{BA}} \in (0,2\pi)+4k\pi \\ \Delta\varphi_{\mathrm{A}} + \dfrac{\Delta\varphi'_{\mathrm{BA}}}{2} + \pi & \Delta\varphi_{\mathrm{BA}} \in (-2\pi,0)+4k\pi \end{cases} \tag{B7}$$

$$\Delta\varphi_{\mathrm{A}} + 2\tan^{-1}\left(\frac{\sin(\Delta\varphi_{\mathrm{BA}}/2)}{1+\cos(\Delta\varphi_{\mathrm{BA}}/2)}\right) = \Delta\varphi_{\mathrm{A}} + \frac{\Delta\varphi'_{\mathrm{BA}}}{2} \tag{B8}$$

So for the case of $0 \leq \rho \leq 1$, we can conclude that

$$\Delta\varphi_{\mathrm{C}} \in \begin{cases} [\Delta\varphi_{\mathrm{A}} + \Delta\varphi'_{\mathrm{BA}}/2 - \pi, \Delta\varphi_{\mathrm{A}} + \Delta\varphi'_{\mathrm{BA}}/2], & \Delta\varphi_{\mathrm{BA}} \in (0,2\pi)+4k\pi \\ [\Delta\varphi_{\mathrm{A}} + \Delta\varphi'_{\mathrm{BA}}/2, \Delta\varphi_{\mathrm{A}} + \Delta\varphi'_{\mathrm{BA}}/2 + \pi], & \Delta\varphi_{\mathrm{BA}} \in (-2\pi,0)+4k\pi \end{cases} \tag{B9}$$

REFERENCES

1. Cumming, I. G. and F. K. Wong, *Digital Processing of Synthetic Aperture Radar Data: Algorithm and Implementation*, Artech House, Norwood, MA, 2005.
2. Henke, D., C. Magnard, M. Frioud, et al., "Moving-target tracking in single-channel wide-beam SAR," *IEEE Trans. on Geosci. Remote Sens.*, Vol. 50, No. 11, 4735–4747, 2012.
3. Mouche, A. A., F. Collard, B.Chapron, et al., "On the use of doppler shift for sea surface wind retrieval from SAR," *IEEE Trans. on Geosci. Remote Sens.*, Vol. 50, No. 7, 2901–2909, 2012.
4. Zhou, J. X., Z. G. Shi, X. Cheng, et al., "Automatic target recognition of SAR imagesbased on global scattering center model," *IEEE Trans. on Geosci. Remote Sens.*, 3713–3729, 2011.
5. Papson, S. and R. M. Narayanan, "Classification via the shadow region in SAR imagery," *IEEE Trans. on Aerospace and Electronic Systems*, Vol. 48, No. 2, 969–980, 2012.
6. Dabboor, M., M. J. Collins, V. Krrathanassi, et al., "An unsupervised classification approach for polarimetric SAR data based on the chernoff distance for complex wishart distribution," *IEEE Trans. Geosci. Remote Sens.*, Vol. 51, No. 7, 4200–4213, 2013.
7. Zhu, X. X. and R. Bamler, "Tomographic SAR inversion by L_1-norm regularization — The Compressive Sensing Approach," *IEEE Trans. Geosci. Remote Sens.*, Vol. 48, No. 10, 3839–3846, 2010.
8. Xing, S. Q., Y. Z. Li, D. H. Dai, et al., "Three-dimensional reconstruction of man-made objects using polarimetric tomographic SAR," *IEEE Trans. Geosci. Remote Sens.*, Vol. 51, No. 6, 3694–3705, 2013.
9. Rosen, P. A., S. Hensley, I. R. Joughin, et al., "Synthetic aperture radar interferometry," *Proc. IEEE*, Vol. 88, No. 3, 333–382, 2000.
10. Berardino, P., G. Fornaro, R. Lanari, et al., "A new algorithm for surface deformation monitoring based on small baseline differential SAR interferograms," *IEEE Trans. Geosci. Remote Sens.*, Vol. 40, No. 11, 2375–2383, 2002.
11. Cloude, S. R. and K. P. Papathanassiou, "Polarimetric SAR interferometry," *IEEE Trans. Geosci. Remote Sens.*, Vol. 36, No. 5, 1551–1565, 1998.
12. Papathanassiou, K. P. and S. R. Cloude, "Single baseline polarimetric SAR interferometry," *IEEE Trans. Geosci. Remote Sens.*, Vol. 39, No. 11, 2352–2363, 2001.
13. Zhu, X. X. and R. Bamler, "Demonstration of super-resolution for tomographic SAR imaging in urban environment," *IEEE Trans. Geosci. Remote Sens.*, Vol. 50, No. 8, 3150–3157, 2012.
14. Austin, C. D. and R. L. Moses, "IFSAr processing for 3D target reconstruction," *Algorithms for Synthetic Aperture Radar Imagery XII, SPIE Defense and Security Symposium, Orlando*, 2005.
15. Austin, C. D. and R. L. Moses, "Interferometric synthetic aperture radar detection and estimation based 3D image reconstruction," *Algorithms for Synthetic Aperture Radar Imagery XIII, SPIE Defense and Security Symposium, Orlando*, 2006.
16. Xing, S. Q., "Study on the 3D imaging of manmade target based on polarimetric radar," *ChinaNational University of Defense Technology*, 2013.
17. Pauciullo, A., D. Reale, A. D. Maio, et al., "Detection of double scatterers in SAR tomography," *IEEE Trans. Geosci. Remote Sens.*, Vol. 50, No. 9, 3567–3586, 2012.
18. Lombardini, F. and M. Pardini, "Superresolution differential tomography: Experiments on identification of multiple scatterers in spaceborne SAR data," *IEEE Trans. Geosci. Remote Sens.*, Vol. 50, No. 4, 1117–1129, 2012.
19. Burrows, M. L., "Two-dimensional ESPRIT with tracking for radar imaging and feature extraction," *IEEE Trans. Antenna Propagat.*, Vol. 52, No. 2, 524–532, 2004.